Probing potential energy surfaces with high-resolution spectroscopy

From the Universe's carbon locker to molecular machines

Maltseva, E.O.

Publication date
2017

Document Version
Other version

License
Other

CHAPTER 5

Vibrationally-resolved spectroscopic studies of electronically excited states of 1,8-naphthalic anhydride and 1,8-naphthalimide: A delicate interplay between one $\pi\pi^*$ and two nπ^* states

Abstract

The spectroscopic and dynamic properties of the lower electronicaly excited states of 1,8-naphthalic anhydride and 1,8-naphthalimide have been studied in supersonically cooled molecular beams using nanosecond Resonance Enhanced MultiPhoton Ionization (REMPI) spectroscopic techniques in combination with quantum chemical calculations. The excitation spectra of these compounds show near–and even below–the apparent 0-0 transition to a strongly allowed electronic state, previously assigned as the S_1 ($2^1A_1(\pi\pi^*)$) state, a plethora of vibronic transitions that cannot simply be rationalized in terms of Franck-Condon vibronic activity of that particular state. Instead, it is shown that the $^1B_1(n\pi^*)$ state, which previously was reported to be S_3 for vertical excitation, is adiabatically the lowest excited singlet state. Interactions between this "dark" state and the "bright" $2^1A_1(\pi\pi^*)$ state lead to intensity borrowing of transitions to "dark" state levels that thus show up in the excitation spectra. A complicating factor is that, apart from the coupling of these two singlet states, also a relatively strong spin-orbit coupling between the $2^1A_1(\pi\pi^*)$ and $^3B_1(n\pi^*)$ states is present. We show that the latter state has a slightly higher adiabatic excitation energy than the former state in 1,8-naphthalic anhydride but lies energetically below the $2^1A_1(\pi\pi^*)$ state in 1,8-naphthalimide. Concurrently, we find that the decay dynamics of excited states of 1,8-naphthalimide are entirely dominated by intersystem crossing while in 1,8-naphthalic anhydride both internal conversion to the ground state and intersystem crossing occur, albeit that the former loses importance once the excitation energy exceeds that of the $^3B_1(n\pi^*)$ state.[‡]

[‡]This chapter is adopted from E. Maltseva, S. Amirjalayer, W. J. Buma. *Phys. Chem. Chem. Phys.*, **19**, 5861, 2017.

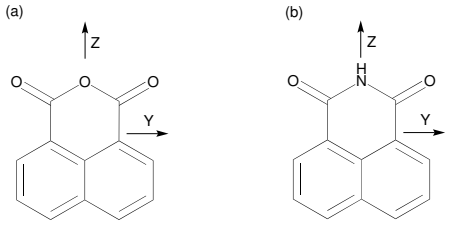

Figure 5.1: Chemical structure of NA (a) and NI (b) with the coordinate axes.

5.1 Introduction

Recent years have witnessed an ever-increasing interest in means to transform photon energy into functionality. To this purpose novel molecular systems are developed that aim to provide efficient and stable platforms for such transformations. The primary step in these transformations is excitation to electronically excited states whose subsequent (non-)radiative decay pathways then serve to reach the desired goal. Understanding the mechanisms of photoexcitation and electronic deactivation is consequently crucial for tailoring and optimizing the performance of such systems.

The present studies focus on the properties of two naphthalene-based heterocyclic compounds, 1,8-naphthalic anhydride (NA) and 1,8-naphthalimide (NI) (Fig.5.1), that serve as the starting point for developing chromophores employed in a wide range of technological applications. Derivatives of NA are extensively used as fluorescent dyes, fluorescent whitening agents and acceptor agents in solar cells.[1–3] The NA molecule is also important as it serves as a model compound for 3,4,9,10-perylenetetracarboxylic diimide and 1,4,5,8-naphthalene-tetracarboxylic dianhydride which are important classes of electroactive and photoactive organic materials as well as a unique class of n-type organic semiconductors.[4–9] NI and its derivatives, on the other hand, have found applications in organic light emitting diodes (OLEDs)[10] and are used as highly fluorescent dyes for biological markers,[11,12] liquid crystal displays[13] while more recent applications involve their use in molecular nanotechnology to power up molecular machines.[14,15]

Seminal studies on the excited-state dynamics of these molecules have recently been performed with picosecond multiphoton ionization spectroscopy on supersonically cooled, isolated molecules in combination with quantum chemical calculations and nonadiabatic dynamics simulations.[16,17] From these studies it was concluded that intersystem crossing (ISC) is a major decay channel in both molecules, mainly as the result of the near-degeneracy of the $S_1(\pi\pi^*)$ and $T_4(n\pi^*)$ states combined with a relatively large spin-orbit coupling between these two states. This decay channel was reported to be dominating the excited-state dynamics in NI, but in NA was deduced to be in competition with internal conversion (IC) to the ground state. Simulations indicated that the internal conversion decay channel is to a large extent dependent on a barrier that needs to be overcome to get access to a conical intersection with the ground state.

In the present work we use frequency-domain studies in combination with nanosecond pump-probe experiments to study the spectroscopic properties of these molecules and their excited-state dynamics. The advantage of this approach is that we are able to obtain excitation spectra with lifetime-limited band widths and not laser-limited band widths as was the case in the ps studies. Similar to the ps studies we employ Resonance Enhanced MultiPhoton Ionization (REMPI) spectroscopic techniques, but instead of a

(1+2') scheme that is liable to suffer from saturation and the influence of electronically excited states at the two-photon level, we use (1+1') RE2PI. Indeed, we find that the increased resolution allows us to record spectra with a much larger vibrational activity than previously observed. Also, UV-UV depletion spectra in combination with ns pump-probe experiments provide key information on the importance of competing decay channels. We combine these vibrationally-resolved experiments with quantum chemical calculations to show that the spectroscopy of the lower-excited state electronic manifold is quite more complex than thought so far, and that the dynamics in this manifold are governed by subtle differences in excitation energies of the lower electronically excited states in the singlet and triplet manifold.

5.2 Methods

5.2.1 Experimental

NA and NI were purchased from Sigma-Aldrich(99% purity) and used without further purification. The employed molecular beam setup and laser systems have been described in detail before.[18] We will therefore provide here only details pertaining to the specific experiments reported in the present studies. In order to obtain enough vapor pressure, samples were heated to 473 K. A mixture of the vapor with 2 bars of argon was then expanded into a vacuum chamber with a pulsed nozzle (General Valve). After skimming the molecular beam NA and NI molecules arrived in the ionization chamber where two-color Resonance Enhanced Two-Photon Ionization (RE2PI) ionization followed by ion detection using a reflectron type time-of-flight spectrometer (R. M. Jordan Co.) took place. In these RE2PI experiments a frequency-doubled Sirah Cobra-Stretch dye laser pumped by a Spectra Physics Lab 190 Nd:YAG laser was used for excitation. Since the excitation energies are less than half of the ionization energy of NA and NI[19] we have employed a Neweks PSX-501 ArF excimer laser (193 nm, 6.42 eV) for the ionization step. Typical excitation and ionization pulse energies were 0.01-0.05 mJ and 3 mJ, respectively. Pump-probe experiments were performed by scanning the time between excitation and ionization lasers with a step size of 1 ns using a delay generator (Stanford Research Systems DG535). To perform UV-UV ion dip spectroscopy a third laser beam provided by a frequency-doubled Sirah Precision Scan dye laser pumped by a Spectra Physics Lab 190 Nd:YAG laser was employed to perform excitation while depletion took place with the previously mentioned Cobra-Stretch dye laser system. In these experiments the depletion laser was fired 200 ns before the excitation and ionization laser systems.

5.2.2 Theoretical

Geometry optimization followed by calculation of the harmonic force fields was performed for ground and electronically excited singlet and triplet states using (Time Dependent) Density Functional Theory (TD-DFT)[20] and the Gaussian09 version D01[21] set of programs. The same program was used for simulating vibrationally-resolved excitation spectra at the Franck-Condon (FC) and Herzberg-Teller (HT) levels of approximation.[22] Exploratory calculations on NA using a variety of functionals and basis sets including those employed in previous studies[16,17] revealed only minor differences for calculations with different basis sets. The choice of functional turned out in this respect to be more important. The states of interest for the present study are either of $\pi\pi^*$ and $n\pi^*$ type.

The latter states have intrinsically a considerable amount of charge transfer character as electron density is transferred from the carbonyl oxygen atoms to the aromatic ring system.[23] One can therefore expect that for these states a proper description of the charge transfer character is required as was indeed observed and led to the use of the CAM-B3LYP functional.[24] In view of these results, subsequent calculations on NA and NI have only been performed at the CAM-B3LYP/6-31G* level. In order to compare the results of these calculations with the experiment, vibrational frequencies have been scaled with a factor of 0.96.[25]

To calculate at a more accurate level the vertical and adiabatic excitation energies of the lowest $^1\pi\pi^*$ and $^1n\pi^*$ states, also more advanced post-Hartree Fock calculations based on the spin-component scaled version of the approximate coupled-cluster singles-and-doubles model (SCS-CC2)[26,27] were used. These calcualtions were performed using the RICC2 module[28,29] as implemented in the TURBOMOLE package[30] together with the cc-pVDZ basis set[31] and the standard auxiliary basis sets.[32]

5.3 Results

5.3.1 1,8-Naphthalic anhydride

Figure 5.2 (bottom panel, black trace) shows the mass-resolved $2^1A_1(\pi\pi^*) \leftarrow S_0$ excitation spectrum of NA measured using (1+1') nanosecond RE2PI. We find the 0-0 origin for this transition at 30268.2 cm^{-1}, close to the value previously reported in the ps experiments on NA under molecular beam conditions.[16] As might be expected from the increased spectral resolution, the spectrum in Figure 5.2 shows many more bands than the (1+2') ps REMPI excitation spectrum.[16] In fact, in the reported frequency range overall 54 bands are observed with rotational contours of low-energy bands spanning about 2.2 cm^{-1}. What would in first instance appear more surprising are the large differences in relative band intensities. In the ps spectrum the 0-0 transition has about the same intensity as transitions to higher-frequency vibronic transitions, while in the ns spectrum the 0-0 transition is by far the most intense band.

The same panel displays the spectrum that is obtained when the ionization laser is delayed by 1 μs (Figure 5.2, bottom panel, blue trace). In the 550-1200 cm^{-1} region the spectrum is very similar to the spectrum obtained without delay, but this is not the case in the 0-550 cm^{-1} region. This can be clearly visualized by plotting the ratio of the intensity of a band in the delayed-ionization measurements to the intensity measured without delay, against excitation energy (Figure 5.2, top panel). A band with a ratio close to 1 implies that there is no difference in the spectra and thus that the lifetime of the state from which ionization took place is of the order of microseconds. Previous ps studies on NA[16] suggest that this state is associated with the triplet manifold. Conversely, bands with a small ratio are associated with levels with a predominant $S_1(2^1A_1(\pi\pi^*))$ character.

Interestingly, there was hardly an indication for ionization from a triplet state in the previously reported (1+2') REMPE ps experiments (although the solution transient absorption experiments did show a state with a lifetime of at least 30 ns that was assigned on the basis of its transient absorption spectrum to the first excited triplet state).[16] Apparently, under the conditions of the ps experiments the ionization cross section of the triplet state is much lower than in the present experiments. We probed the nanosecond time evolution of the excited state manifold in more detail by pump-probe measurements of selected levels in which the time delay between excitation and ionization laser was

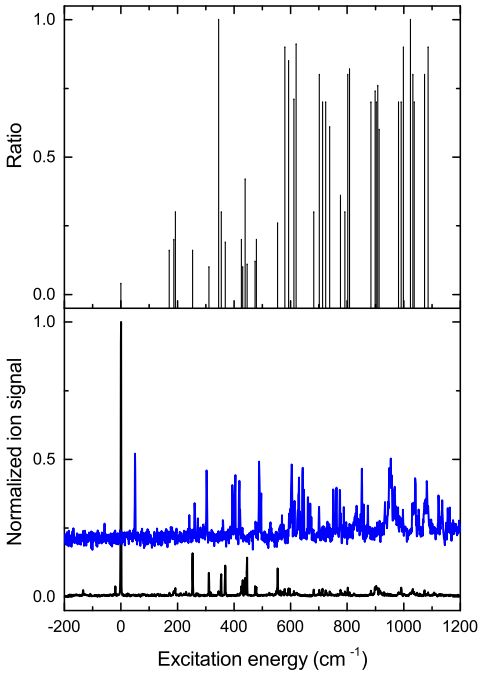

Figure 5.2: Bottom panel: (1+1') RE2PI excitation spectrum of NA. The black and blue traces have been obtained for conditions in which the ionization laser temporally coincides with the excitation laser or is delayed by 1 μs, respectively. For clarity the baseline of the blue trace has been displaced vertically and horizontally and multiplied by 10 in vertical direction. Top panel: ratio between delayed and non-delayed signal intensity (see text). Excitation energy is given with respect to the excitation energy of the 0-0 transition (30268.3 cm^{-1}).

varied. The top panel of Figure 5.3 shows typical time-delay traces obtained at 30268.2 (0-0 transition, black trace), 30521 (+235, red trace) and 31259.8 (+991.6, green trace) cm^{-1}. All traces show a long-lived component but with different relative amplitudes with respect to a short-lived component. The long-lived components appear to show a decay but this decay does not reflect the lifetime of the long-lived state. Instead, it is caused by the drift of excited molecules out of the ionization spot. Once the signal is corrected for this drift it remains constant for at least 2 μs.

The decay observed at the +991.6 cm^{-1} band (Fig. 5.3, green trace), which only shows a long-lived component, is characteristic for almost all of the other bands recorded in the spectrum. In fact, only for low-vibrational energy transitions such as the 0-0 and +235 cm^{-1} bands a decay trace is observed that shows a fast nanosecond component attributed to the convolution of the two nanosecond laser pulses around zero time delay. Such a convolution can only be observed if the accessed excited state lives long enough

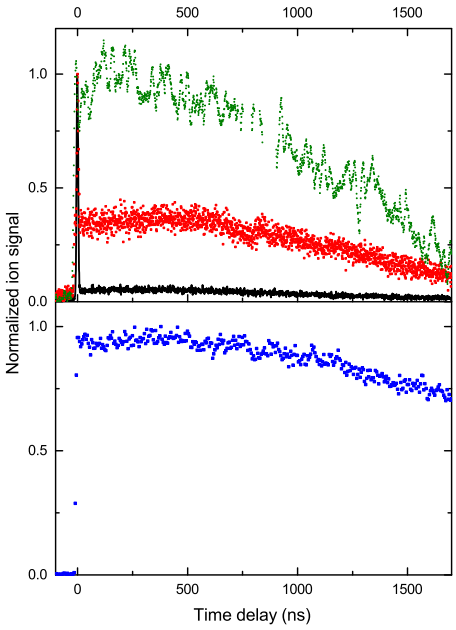

Figure 5.3: Time-delay traces of (1+1') RE2PI signals at various excitation energies. Top and bottom panels display traces for NA and NI, respectively. Time zero corresponds to no delay between excitation and ionization lasers.

to show ionization from the singlet level. With an excess of vibronic energy the lifetime of the $S_1(\pi\pi^*)$ state drops rapidly. As a result, ionization from the singlet level becomes suppressed and ionization from the long-lived state dominates. This decrease in lifetime could be either due to a sharp increase of the ISC rate to the triplet manifold or of the IC rate to the ground state. Previously, it was tentatively concluded that the latter occurs, here we will argue on the basis of the present experiments and calculations in favour of the former explanation (vide infra).

Further information on the excited-state dynamics is obtained from UV-UV ion-depletion spectroscopy. The bottom panel of Figure 5.4 displays the UV-UV depletion spectrum in the same region as reported in Figure 5.2, while Table 5.2 in the Supporting Information reports the positions of the major bands in this spectrum. Before interpreting this spectrum in more detail, it is useful to consider how a long-lived state affects a UV-UV depletion spectrum.[33] Molecules in such a state remain excited during the time interval between depletion and detection after the depletion laser pulse ends, and can therefore still contribute to the ion signal that is monitored in the detection step. In contrast, the ionization cross section of molecules that undergo internal conversion to the electronic ground state is generally close to zero and they should be considered as being "dark" for detection. Although in the present case the exact contribution of triplet-state molecules to the detection signal clearly depends on details such as the relative

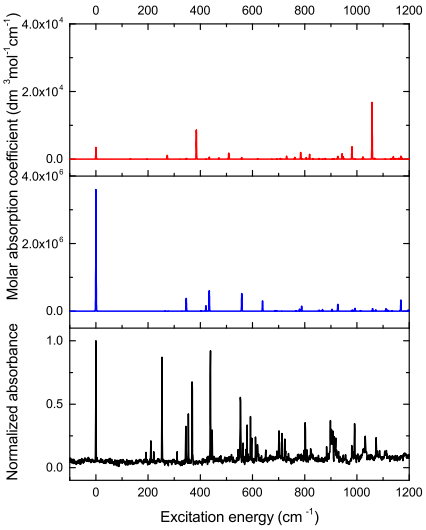

Figure 5.4: Bottom panel: UV-UV depletion spectrum of NA using the 0-0 transition to monitor $S_1 \leftarrow S_0$ absorption. Middle panel: absorption spectrum of NA predicted at the Franck-Condon (FC) level of approximation. Top panel: $2^1A_1(\pi\pi^*) \leftarrow S_0$ absorption spectrum of NA predicted at the Herzberg-Teller (HT) level of approximation. Spectra are reported with respect to the 0-0 transition at 30268.3 cm^{-1}.

ionization cross sections from singlet and triplet states as well as IC and ISC rates, the most straightforward explanation for a decrease of the detection signal is that molecules have undergone internal conversion to the ground state. Figure 5.4 shows that in the UV-UV depletion spectrum a decrease of the signal is observed for all bands, also for bands for which Figure 5.2 does not show a difference between delayed and non-delayed signal intensity. As reasoned above, this implies that also at these excitation energies IC to the ground state is still a relevant decay channel even though the ns time-delay traces would seem to indicate that the ISC channel completely dominates the decay of the S_1 levels.

Figure 5.2 and the bottom panel of Figure 5.4 show the same bands but with quite different intensities in the low-energy region, in particular for the 0-0 transition that has now become of similar intensity as other strong bands. In fact, the overall appearance of the spectrum is quite similar to the spectrum reported previously with ps excitation. The middle spectrum in Figure 5.4 shows the absorption spectrum predicted at the Franck-Condon level of approximation (see Table 5.3 for calculated vibrational frequencies). This spectrum is characterized by a strong 0-0 transition and minor activities of totally-symmetric modes with a_1 modes 20-16 being the more prominent. Although these activities can be recognized in the experimental spectrum, it is also immediately clear that there are significant differences. These concern the relative intensity of the origin transition and the large number of bands in the experimental spectrum that are not

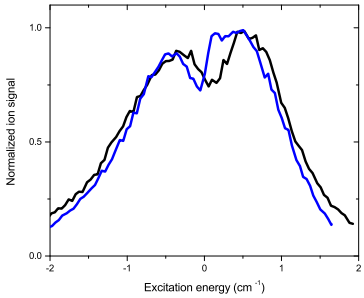

Figure 5.5: Experimental rotational contours of the 0-0 (black trace) and +253.3 cm^{-1} (blue trace) bands.

predicted by the calculations. Moreover, the lowest-frequency totally-symmetric mode $20a_1$ is assigned to the 368.3 cm^{-1} band, but the experiment shows at least 7 more bands at lower vibronic energies that cannot be reconciled with overtone or combination bands of non-totally symmetric vibrations.

Our calculations predict that the Franck-Condon factor for the 0-0 transition is at least five times larger than that of transitions to higher vibronic levels (see middle spectrum in Figure 5.4) irrespective of the level at which they were performed. We therefore conclude that the differences between experiment and theory are due to differences in the excited-state dynamics of these levels. IC to the ground state populates levels that are "dark" for ionization and thus lead to a reduction of the REMPI signal. ISC, on the other hand, populates long-lived triplet levels that are "bright" for ionization. Our studies thus demonstrate that near the vibrationless level in the excited state electronic deactivation are dominated by IC to the ground state, while for higher vibronic levels (roughly above $\sim$300 cm^{-1}) ISC is the dominant decay channel.

A possible explanation for the observed non-Franck-Condon activity could be vibronic coupling to higher-lying electronic states which would induce activity of transitions to non-totally symmetric vibrational levels. Indeed, we find that the strong band at 253.3 cm^{-1} band is close to the frequency calculated for the $19b_2$ mode (273 cm^{-1}) of the $2^1A_1(\pi\pi^*)$ state suggesting that this band is a false origin band, that is, a band that acquires intensity from vibronic coupling and acts as an origin band upon which totally-symmetric progressions are built. Support for such a conclusion is provided by comparing the rotational contours of the 253.3 cm^{-1} and origin bands depicted in Figure 5.5. These show clear differences and one thus has to conclude that the two bands involve differently oriented electronic transition moments.

To further investigate the role of vibronic coupling, we have calculated the absorption spectrum at the Herzberg-Teller level of approximation in which bands derive their intensity only from vibronic coupling and not from the direct $2^1A_1(\pi\pi^*) \leftarrow S_0$ transition moment. Comparison of this HT spectrum (top panel of Figure 5.4) with the FC spectrum (middle panel) shows that vibronically-induced transitions are predicted to be less strong than direct transitions by about two orders of magnitude. This observation is surprising in view of the previous discussion on rotational contours, but is actually in line with a priori expectations based on transition moments calculated for transitions to

Table 5.1: Adiabatic (AE) and vertical (VE) excitation energies (eV) as well as oscillator strength (f) (at S_0 geometry) of the S_{1-4} and T_{2-5} excited states of NA and NI, calculated at CAM-B3LYP/6-31G* TD-DFT level. Vertical and adiabatic excitation energies calculated at the SCS-CC2/cc-pVDZ level are listed in bold in parentheses

1,8-Naphthalic anhydride			
	AE	**VE**	***f***
S_1 $^1A_1(\pi\pi^*)$	3.97 (**3.97**)	4.25 (**4.12**)	0.2087
S_2 $^1B_2$ $(\pi\pi^*)$	4.32	4.45	0.0413
S_3 $^1B_1$ $(n\pi^*)^\dagger$	4.26 (**3.93**)	4.57 (**4.67**)	0.0003
S_4 $^1A_2$ $(n\pi^*)$	4.68	4.96	0
T_2 $^3B_2$ $(\pi\pi^*)$	3.34	3.55	0
T_3 $^3B_2$ $(\pi\pi^*)$	3.67	3.83	0
T_4 $^3B_1$ $(n\pi^*)$	3.84	4.13	0
T_5 $^3B_2$ $(\pi\pi^*)$	4.46	4.59	0
1,8-Naphthalimide			
	AE	**VE**	***f***
S_1 $^1A_1(\pi\pi^*)$	3.95 (**3.95**)	4.22 (**4.11**)	0.2163
S_2 $^1B_1$ $(n\pi^*)^\dagger$	4.07 (**3.86**)	4.34 (**4.42**)	0.0002
S_3 $^1B_2$ $(\pi\pi^*)$	4.3	4.42	0.033
S_4 $^1A_2$ $(n\pi^*)$	4.53	4.78	0
T_2 $^3B_2$ $(\pi\pi^*)$	3.38	3.57	0
T_3 $^3B_2$ $(\pi\pi^*)$	3.686	3.86	0
T_4 $^3B_1$ $(n\pi^*)$	3.687	3.94	0
T_5 $^3B_2$ $(\pi\pi^*)$	4.08	3.86	0

the lower-lying electronic states (Table 5.1). These show that the transition moment to the $^1B_2(\pi\pi^*)$ state–which would be the most logical candidate for inducing intensities in transitions to b_2 levels–is 5 times smaller than the transition moment to the $2^1A_1(\pi\pi^*)$ state. Combined with the energy gap between the two states, this indeed leads to induced transition moments that are considerably smaller than the direct moment.

Another noteworthy observation comes from rotational contour simulations of the origin and 253.3 cm^{-1} bands using the PGOPHER program.[34] We find that simulations with the rotational constants taken from our calculations on the ground and 2^1A_1 states fail to reproduce the experimental contours. Further studies reveal that this is mainly caused by the changes in the A rotational constant upon excitation, the a inertial axis being parallel with the molecular z-axis (Fig.5.1). Calculations predict that A is reduced upon excitation, but simulations in which A is slightly increased show a much better agreement with the experiment. It would thus appear that at the TD-DFT level of theory the geometry of the $2^1A_1(\pi\pi^*)$ state is not predicted correctly. Since TD-DFT fails in case of strong couplings between electronic states, these observations might be taken as an indication that the $2^1A_1(\pi\pi^*)$ state is perturbed by other electronic states.

†Both NA and NI adopt in the $^1B_1$ $(n\pi^*)$ state a planar equilibrium geometry of C_s symmetry. Formally, this state should therefore be referred to as the $^1A''$ $(n\pi^*)$ state. For clarity, however, we continue to label it with its $C_{2\nu}$ symmetry label.

5.3.2 1,8-Naphthalimide

The bottom panel of Figure 5.6 shows the $S_1 \leftarrow S_0$ excitation spectrum of NI obtained with (1+1') RE2PI. Overall, 64 bands with rotational contour widths of about 2.5 cm^{-1} can be distinguished in the reported energy region, the positions of the major bands being given in Table 5.2 in the Supporting Information. The spectrum displays a strong band at 30062.5 cm^{-1}, but also several weaker bands at lower excitation energies (e.g. 29919.5, 29925.8, 29934.7, 29938.3, 29953.5, 29960.7 and 30015.6 cm^{-1}). Since one expects the electronic structure of NA and NI to be similar–and thus no major changes in the relative intensity of the 0-0 band of the $2^1A_1(\pi\pi^*) \leftarrow S_0$ transition–we assign the 30062.5 cm^{-1} as the 0-0 band. This value differs 20 cm^{-1} from the value reported in (1+2') ps REMPI experiments[17] (30082 cm^{-1}) but this can be due to the fact that the bands in the latter spectrum are rather broad. The ps spectrum showed activity below the assigned 0-0 transition as well, but the present experiments make clear that the single band reported in those studies to be below the 0-0 band actually consists of several transitions that have now become resolved. In view of the similarity of their electronic structure, one would expect that the vibrational activity in the excitation spectra of NA and NI to be comparable. This is not sustained in the experiments that show a multitude of close-lying transitions in the 150-250 cm^{-1} region above the 0-0 transition. Also, although some narrow bands can be distinguished, it would appear that at higher vibrational energies bands are broader and/or consist as well of overlapping transitions. Finally, in NA vibrational activity extends to over 1000 cm^{-1} but quickly disappears above 400 cm^{-1} in NI. The vibrational activity predicted for the $2^1A_1(\pi\pi^*) \leftarrow S_0$ transition within the FC approximation is displayed in the middle panel of Figure 5.6. As expected, this spectrum reproduces to a large extent the spectrum predicted for NA (middle panel Figure 5.4) but hardly bears any resemblance to the experimentally observed vibrational activity. The top panel of Figure 5.6 shows the spectrum that is predicted within the HT approximation. Similar to NA, vibronically induced intensities are found to be two orders of magnitude smaller than those associated with the direct transition to the $2^1A_1(\pi\pi^*)$ state. Theory thus finds NA and NI to be spectroscopically similar, but this is not reproduced by our experimental observations. For NA we concluded on the basis of its rotational contour that the strong band at 253.3 cm^{-1} is associated with a false origin of b_2 symmetry ($19b_2$). For NI the analogous mode ($20b_2$) is predicted to occur at 272 cm^{-1} and indeed we find in the experimental spectrum a similarly strong band at 242.3 cm^{-1} with a b_2 contour, once again much stronger than would be expected on the basis of the HT calculations.

The bottom panel of Fig. 5.3 shows the time-delay trace observed after excitation of the 0-0 band. In contrast to NA for which excitation at, or close to, the vibrationless level leads to decay traces with a short and long-lived component, this trace only shows a long-lived component that loses intensity because the excited molecules drift out of the ionization region. Identical traces are observed after excitation of the strong +242.3 and +322.5 cm^{-1} bands as well as several other weaker bands. From these experiments we can thus conclude that the lifetime of excited $2^1A_1(\pi\pi^*)$ levels is so short that ionization from these levels can no longer be observed as otherwise we would have seen a similar spike for zero time delay as for low-lying levels in NA. Further information on the decay channels is provided by UV-UV ion-depletion experiments which do not show any depletion of the probe signal irrespective of the pump or probe excitation energies. This implies that there is no population loss from the electronically excited manifold in the time interval between pump and probe. This, in turn, leads to the conclusion that the IC rate to S_0

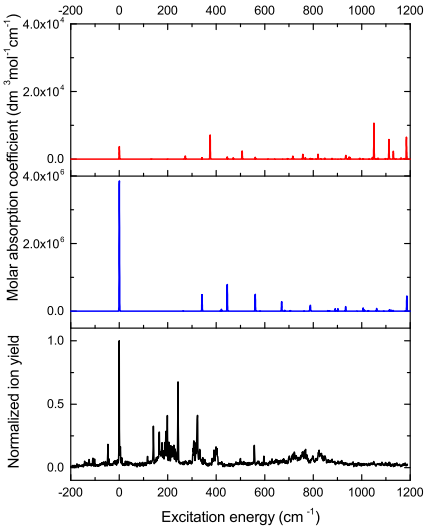

Figure 5.6: Bottom panel: (1+1') REMPI excitation spectrum of NI. Middle panel: absorption spectrum of NI predicted at the Franck-Condon (FC) level of approximation. Top panel: $2^1A_1(\pi\pi^*) \leftarrow S_0$ absorption spectrum of NI predicted at the Herzberg-Teller (HT) level of approximation. Spectra are reported with respect to the band at 30062.5 cm^{-1} which is assigned to the 0-0 band of the $2^1A_1(\pi\pi^*) \leftarrow S_0$ transition.

is negligible compared to the rate with which the triplet state is populated. Apparently, excitation of NI leads to a nearly 100% yield of the triplet state that is observed in the ionization step irrespective of the vibronic level that is excited. Such a conclusion is in line with triplet yields determined in spectroscopic studies on NI in solution.[35]

5.4 Discussion

The (1+1') nanosecond RE2PI experiments on NA and NI discussed above have led to a number of important observations with respect to vibronic activity and excited-state dynamics. To start with the latter: the ps studies on NA showed a sharp decrease in lifetime of excited-state vibronic levels with vibrational energies up to about 400 cm^{-1}. At that time it was suggested that this was caused by a barrier that needed to be overcome in order to access the conical intersection with the ground state, although the small energy range over which the decrease occurs would not seem to be compatible with the estimated height of this barrier (0.7-0.9 eV). Our decay traces and UV-UV depletion experiments, on the other hand, indicate that the decrease is due to a rapid increase of the ISC rate compared to the IC rate to the ground state. For NI both ps and ns experiments show decay dynamics completely dominated by ISC that are independent of the excess vibrational energy in the excited state.

Previous studies reported vertical excitation energies of the lower-lying electronically excited singlet and triplet states of NA and NI.[16,17] These calculations showed that in both molecules the $S_1(2^1A_1(\pi\pi^*))$ and $T_4(^3B_1(n\pi^*))$ states are nearly degenerate. In agreement with El-Sayed rules[36] it was found that the spin-orbit coupling matrix element between these two states ($\sim$10 cm^{-1}) is several orders of magnitude larger than spin-orbit couplings between the $S_1(2^1A_1(\pi\pi^*))$ and $^3\pi\pi^*$ states. Since for the present study knowledge of the adiabatic excitation energies of the lower excited singlet and triplet manifold is important (vide infra), we have extended these calculations–albeit with a slightly different basis set–to include adiabatic excitation energies as well (see Table 5.1). These calculations show excellent agreement with the previous studies as far as the vertical excitation energies are concerned, and show that the quasi-degeneracy of the $S_1(2^1A_1(\pi\pi^*))$ and $T_4(^3B_1(n\pi^*))$ states is maintained at the adiabatic level. Importantly, the Table 5.1 also shows that for both vertical and adiabatic excitation the energy gap between the two states increases upon going from NA to NI. In fact, with the def2-TZVP basis the $T_4(^3B_1(n\pi^*))$ state is calculated to be slightly higher than the $S_1(2^1A_1(\pi\pi^*))$ state while for NI it is slightly lower. In view of these observations we attribute the sharp drop in lifetime in NA to the fact that at these excitation energies the ISC decay pathway to the $T_4(^3B_1(n\pi^*))$ state opens up. In contrast, for NI this decay channel is already available starting from the vibrationless level in the excited state, and for this molecule one therefore does not see a vibronic energy dependence of the lifetime.

With regard to the vibronic activity, the intrinsically better spectral resolution of the present studies has made it clear that almost all of the bands in the excitation spectra reported in ps REMPI experiments actually consist of several overlapping transitions. Moreover, the rising background that was present in the ps excitation spectra is absent in the ns spectra. We have made careful studies of the power dependence of the bands in our ns spectra to ensure that these spectra are not affected by saturation as this was a point of concern in the ps spectra that are more prone to be saturated. The intensities of bands in the ns spectra thus are real and not distorted by experimental conditions. In agreement with a priori expectations, calculations predict only a limited and low-intensity vibrational activity in the $2^1A_1(\pi\pi^*) \leftarrow S_0$ excitation spectrum, which moreover should be very similar for NA and NI. This is, however, not what is observed experimentally.

We find that attempts to assign bands in the experimental spectrum purely on the basis of calculated frequencies rapidly fail. The number of levels that can reasonably be expected to be accessible is simply not high enough to account for all bands, in particular in the low-energy region of NI. Also finding combination bands in the experimental spectrum of high-intensity transitions that normally would be expected to be observable does not work out as the calculated frequency for the combination band is nearly always found to deviate too much from bands close to this frequency to justify such an assignment. Finally, we recall that the excitation spectrum of NI features several transitions at lower energies than the assigned 0-0 transition. Normally, one would suspect that these bands are hot bands but the vibrational frequencies that have been calculated for the ground and $2^1A_1(\pi\pi^*)$ state do not support this. Experimentally, we arrive at the same conclusion in experiments in which carrier gas and expansion conditions are changed. All these observations lead to the conclusion that the bands observed in the excitation spectra of NA and NI are not only associated with the $2^1A_1(\pi\pi^*) \leftarrow S_0$ transition, but involve transitions to another electronic state as well. Moreover, based on the presence of bands that cannot be accounted for it would appear that this state has a lower adiabatic excitation energy in NI than in NA.

Above it has been discussed that in both molecules the $S_1(2^1A_1(\pi\pi^*))$ and $T_4(^3B_1(n\pi^*))$

states are nearly degenerate and that the spin-orbit coupling matrix element between these two states is sizable. In first instance one might therefore think that the $T_4(^3B_1(n\pi^*))$ state could be responsible for the additional transitions observed in the $S_1 \leftarrow S_0$ excitation spectra. Transitions to these levels are normally forbidden but would acquire oscillator strength by extensive mixing with the nearly degenerate $2^1A_1(\pi\pi^*)$ state. The problem with this explanation is that the $T_4(^3B_1(n\pi^*))$ state is in turn strongly coupled to the lower-lying $T_{3,2,1}$ states with nonadiabatic coupling matrix elements that are up to almost two orders of magnitude larger than the $S_1(2^1A_1(\pi\pi^*))$-$T_4(^3B_1(n\pi^*))$ coupling. Under such conditions one does not expect sharp bands with always about the same width. We therefore conclude that the state responsible for the additional bands must be another singlet state.

Table 5.1 shows that at the TD-DFT level one of the possible candidates for this state, the $^1B_1(n\pi^*)$ state, is adiabatically close to the $2^1A_1(\pi\pi^*)$ state with an energy difference between the two states that decreases upon going from NA to NI, but still remaining above the $2^1A_1(\pi\pi^*)$ state. In view of the partial charge-transfer character of this state, it might very well be that calculations at a higher level are needed for a proper description of this state and its excitation energy. We have therefore repeated calculations of the vertical and adiabatic excitation energies of these two states at the SCS-CC2/cc-pVDZ level. Vertically, the $^1B_1(n\pi^*)$ state remains higher than the $2^1A_1(\pi\pi^*)$ state with excitation energies that are nearly the same as calculated at the TD-DFT level. The adiabatic excitation energy of the $^1B_1(n\pi^*)$ state is, however, lowered considerably. In excellent agreement with our experimental observations we find that in NA the $2^1A_1(\pi\pi^*)$ and $^1B_1(n\pi^*)$ states are for all practical purposes degenerate, while in NI the $^1B_1(n\pi^*)$ state is clearly lower. We thus conclude (a) that the state that is responsible for the additional bands in the excitation spectrum is the $^1B_1(n\pi^*)$ state, and (b) that this state is adiabatically the lowest excited singlet state in NI while in NA it probably has its 0-0 transition slightly above the 0-0 transition of the $2^1A_1(\pi\pi^*)$ state.

We have tried to come to a further assignment of the bands in the excitation spectra of NA and NI by calculating the vibrational activity expected for the $^1B_1(n\pi^*) \leftarrow S_0$ transition. Fig. 5.7 displays to this purpose spectra predicted at the FC and HT levels of approximation. The oscillator strength of the transition to the $^1B_1(n\pi^*)$ state is three orders of magnitude smaller than that of the transitions to the $2^1A_1(\pi\pi^*)$ state. We therefore expect that the former transition acquires its transition intensity to a large extent from coupling to the $2^1A_1(\pi\pi^*)$ state as is confirmed by comparing the intensities in the FC and HT spectra. However, overall these intensities are considerably smaller than those calculated for the $2^1A_1(\pi\pi^*) \leftarrow S_0$ transition (Figures 5.4 and 5.6). On hindsight this is not so surprising since the small energy separation between the $^1B_1(n\pi^*)$ and $2^1A_1(\pi\pi^*)$ states makes the use of the HT approach questionable; very likely a full non-adiabatic coupling approach needs to be used to properly describe the coupling of the two states. This most likely is also the reason that so far we have not succeeded in making unambiguous assignments of bands in the experimental spectra to specific vibronic transitions to the $^1B_1(n\pi^*)$ state.

Vibronic interactions between the $2^1A_1(\pi\pi^*)$ and $^1B_1(n\pi^*)$ states are important to understand the excitation spectra of NA and NI, but we notice that these spectra show that the $2^1A_1(\pi\pi^*)$ is vibronically coupled to the $^1B_2(\pi\pi^*)$ state as well. We have identified unambiguously one of the associated false origin bands, and also for some other reasonably intense bands we have reason to believe that they are associated with false origins. These bands have an unexpectedly high intensity that so far cannot be rationalized on the basis of the oscillator strengths of the transitions to the involved

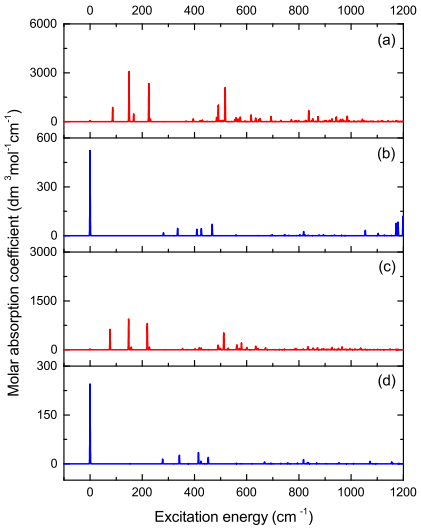

Figure 5.7: Panels (a) and (c): $^1B_1(n\pi^*) \leftarrow S_0$ absorption spectra of NA and NI predicted at the Herzberg-Teller (HT) level of approximation. Panels (b) and (d): $^1B_1(n\pi^*) \leftarrow S_0$ absorption spectra of NA and NI predicted at the Franck-Condon (FC) level of approximation. Spectra are reported with respect to the 0-0 origin transition of the $^1B_1(n\pi^*) \leftarrow S_0$ transition.

states. Further quantum chemical work will be needed to come to a full understanding of this coupling pathway.

5.5 Conclusions

Vibrationally-resolved laser spectroscopic studies and quantum chemical calculations have been employed to study the spectroscopy and dynamics of the lower-excited state manifold of 1,8-naphthalic anhydride and 1,8-naphthalimide. The overall picture that arises from these studies is a complicated one with three major actors that are energetically quasi-degenerate: the strongly absorbing $2^1A_1(\pi\pi^*)$ state, the weakly-absorbing $^1B_1(n\pi^*)$ state, and the spin-forbidden $^3B_1(n\pi^*)$ state. Due to a relatively strong spin-orbit coupling between the $2^1A_1(\pi\pi^*)$ and $^3B_1(n\pi^*)$ states, intersystem crossing is an important decay channel in both molecules, although how this works out in detail shows subtle differences between the two molecules. In NI the $^3B_1(n\pi^*)$ state has a lower excitation energy than the $2^1A_1(\pi\pi^*)$ state, and an almost unit intersystem crossing quantum yield to the triplet state is found. In NA, on the other hand, the $^3B_1(n\pi^*)$ state is concluded to be a few hundred cm^{-1} higher in energy than the $2^1A_1(\pi\pi^*)$ state. As a result, internal conversion to the ground state is the dominant decay channel for excitation energies close to the vibrationless origin and intersystem crossing only sets in at higher excitation energies. Interestingly, it is found that also at these higher excitation energies

internal conversion to the ground state continues to be an observable decay channel.

The resolution in the obtained excitation spectra of NA and NI has enabled us to conclude that these spectra cannot be simply explained in terms of direct and/or vibronically induced transitions to the $2^1A_1(\pi\pi^*)$ state. In combination with high-end quantum chemical calculations we have shown that the general ideas on the state ordering of the lower electronic manifold of these compounds needs a major revision. The $2^1A_1(\pi\pi^*)$ state is not the isolated, adiabatically lowest state thought so far, but is almost degenerate with the $^1B_1(n\pi^*)$ state in NA, while in NI the $\pi\pi^*$ is definitely energetically higher than the $n\pi^*$ state. This is an important conclusion because it implies that under non-isolated conditions a solvent could very well have a larger influence on the the excited-state dynamics of these two compounds and their derivatives than assumed so far, in particular for more polar solvents where the $\pi\pi^*$ and the $n\pi^*$ state are expected to undergo a red- and blue-shift, respectively. Similar drastic changes in decay dynamics due to such shifts have recently been reported for sunscreen components.[37] Likewise, one can envisage that it should be possible to fine-tune the properties of these chromophores even by substituents that are normally considered as non-perturbative.

The assignment of bands in the excitation spectra of NA and NI to state-specific vibronic transitions remains a major challenge. It is, however, one to pursue as similar situations with several closeby, interacting states are increasingly being reported. To disentangle such spectra, complementary spectroscopic techniques will need to be used that allow one to project levels accessed in the excited state on another vibronic manifold that is more easy to assign. One such a strategy is kinetic-energy-resolved photoelectron detection in which the ionic manifold serves as template to characterize excited-state vibronic levels.[18,38,39] Such studies are presently being performed.

References

1. I. Grabtchev. *Dyes Pigm.*, **27**, 321, 1995.
2. Q. Xuhong, Z. Zhenghua, C. Kongchang. *Dyes Pigm.*, **11**, 13, 1989.
3. X. Zhang, J. Zhang, H. Lu, J. Wu, G. Li, C. Li, S. Li, Z. Bo. *J. Mater. Chem. C*, **3**, 6979, 2015.
4. S. K. Lee, Y. Zu, A. Herrmann, Y. Geerts, K. Müllen, A. J. Bard. *J. Am. Chem. Soc.*, **121**, 3513, 1999.
5. G. Seybold, G. Wagenblast. *Dyes Pigm.*, **11**, 303, 1989.
6. D. Schlettwein, D. Woehrle, E. Karmann, U. Melville. *Chem. Mater.*, **6**, 3, 1994.
7. M. Sadrai, L. Hadel, R. R. Sauers, S. Husain, K. Krogh-Jespersen, J. D. Westbrook, G. R. Bird. *J. Phys. Chem.*, **96**, 7988, 1992.
8. C. Falkenberg, C. Uhrich, S. Olthof, B. Maennig, M. K. Riede, K. Leo. *J. Appl. Phys.*, **104**, 034506, 2008.
9. C. K. Chan, E. G. Kim, J. L. Brédas, A. Kahn. *Adv. Funct. Mater.*, **16**, 831, 2006.
10. D. Kolosov, V. Adamovich, P. Djurovich, M. E. Thompson, C. Adachi. *J. Am. Chem. Soc.*, **124**, 9945, 2002.
11. E. H. Buhl, J. Lübke. *Neuroscience*, **28**, 3, 1989.
12. W. W. Stewart. *Cell*, **14**, 741, 1978.
13. I. Grabchev, I. Moneva, V. Bojinov, S. Guittonneau. *J. Mater. Chem.*, **10**, 1291, 2000.
14. Q. C. Wang, D. H. Qu, J. Ren, K. Chen, H. Tian. *Angew. Chem., Int. Ed.*, **43**, 2661, 2004.
15. M. R. Panman, P. Bodis, D. J. Shaw, B. H. Bakker, A. C. Newton, E. R. Kay, A. M. Brouwer, W. Jan Buma, D. A. Leigh, S. Woutersen. *Science*, **328**, 1255, 2010.
16. T. Gerbich, H. C. Schmitt, I. Fischer, J. Petersen, J. Albert, R. Mitrić. *J. Phys. Chem. A*, **119**, 6006, 2015.
17. T. Gerbich, H. C. Schmitt, I. Fischer, R. Mitrić, J. Petersen. *J. Phys. Chem. A*, **120**, 2089, 2016.
18. S. Smolarek, A. Vdovin, A. Rijs, C. A. van Walree, M. Z. Zgierski, W. J. Buma. *J. Phys. Chem. A*, **115**, 9399, 2011.
19. A. Bigotto, V. Galasso, G. Distefano, A. Modelli. *J. Chem. Soc., Perkin Trans.* **2**, 1502, 1979.
20. F. Furche, R. Ahlrichs. *J. Chem. Phys.*, **117**, 7433, 2002.
21. M. J. Frisch, G. W. Trucks, H. B. Schlegel, G. E. Scuseria, M. A. Robb, J. R. Cheeseman, G. Scalmani, V. Barone, B. Mennucci, et al. *Gaussian 09, Rev D.01*
22. F. Santoro, A. Lami, R. Improta, J. Bloino, V. Barone. *J. Chem. Phys.*, **128**, 224311, 2008.
23. P. Kucheryavy, G. Li, S. Vyas, C. Hadad, K. D. Glusac. *J. Phys. Chem. A*, **113**, 6453, 2009.
24. T. Yanai, D. P. Tew, N. C. Handy. *Chem. Phys. Lett.*, **393**, 51, 2004.
25. I. M. Alecu, J. Zheng, Y. Zhao, D. G. Truhlar. *J. Chem. Theory Comput.*, **6**, 2872, 2010.
26. O. Christiansen, H. Koch, P. Jørgensen. *Chem. Phys. Lett.*, **243**, 409, 1995.

27. A. Hellweg, S. A. Grün, C. Hättig. *Phys. Chem. Chem. Phys.*, **10**, 4119, 2008.
28. C. Hättig, F. Weigend. *J. Chem. Phys.*, **113**, 5154, 2000.
29. C. Hättig, A. Hellweg, A. Köhn. *Phys. Chem. Chem. Phys.*, **8**, 1159, 2006.
30. TURBOMOLE V6.1 2009: a development of University of Karlsruhe and Forschungszentrum Karlsruhe GmbH, 1989-2007, TURBOMOLE GmbH, since 2007.
31. A. K. Wilson, D. E. Woon, K. A. Peterson, T. H. Dunning. *J. Chem. Phys.*, **110**, 7667, 1999.
32. F. Weigend, A. Köhn, C. Hättig. *J. Chem. Phys.*, **116**, 3175, 2002.
33. M. A. Trachsel, T. Wiedmer, S. Blaser, H. M. Frey, Q. Li, S. Ruiz-Barragan, L. Blancafort, S. Leutwyler. *J. Chem. Phys.*, **145**, 134307, 2016.
34. C. M. Western. PGOPHER: A program for simulating rotational, vibrational and electronic spectra. *J. Quant. Spectrosc. Radiat. Transf.*, **186**, 221, 2016.
35. A. Samanta, B. Ramachandram, G. Saroja. *J. Photochem. Photobiol., A*, **101**, 29, 1996.
36. M. A. El-Sayed. *Acc. Chem. Res.*, **1**, 8, 1968.
37. E. M. M. Tan, M. Hilbers, W. J. Buma. *J. Phys. Chem. Lett.*, **5**, 2464, 2014.
38. M. D. Groo, W. J. Buma. *J. Chem. Phys.*, **127**, 104301, 2007.
39. R. A. Rijkenberg, W. J. Buma. *J. Phys. Chem. A*, **106**, 3727, 2002.

5.6 Supporting information

Table 5.2: Excitation energies (E) and normalized intensities (I) of bands observed in the 30260-31400 cm^{-1} region of 1,8-naphthalic anhydride and 29910-30910 cm^{-1} region of 1,8-naphthalimide

1,8-naphthalic anhydride			**1,8-naphthalimide**		
E (cm^{-1})	**E* (cm^{-1})**	**I**	**E (cm^{-1})**	**E* (cm^{-1})**	**I**
30268.2	0	1	29919.5	-143	0.05
30460.1	191.9	0.12	29925.8	-136.7	0.04
30478.7	210.5	0.2	29934.7	-127.8	0.05
30489.8	221.6	0.13	29938.3	-124.2	0.05
30521.5	253.3	0.87	29953.5	-109	0.07
30579.4	311.2	0.13	29960.7	-101.8	0.06
30613.1	344.9	0.33	30015.6	-46.9	0.18
30622.4	354.2	0.42	30062.5	0	1
30636.5	368.3	0.68	30067	4.5	0.16
30705.1	436.9	0.92	30073.4	10.9	0.08
30713.7	445.5	0.3	30178.6	116.1	0.08
30801.6	533.4	0.55	30203.2	140.7	0.32
30832	563.8	0.19	30227	164.5	0.26
30843.5	575.3	0.14	30237.9	175.4	0.18
30847.3	579.1	0.34	30244.3	181.8	0.15
30860.6	592.4	0.4	30249.8	187.3	0.18
30865.3	597.1	0.23	30254.4	191.9	0.3
30879.6	611.4	0.24	30260.8	198.3	0.39
30887.3	619.1	0.18	30267.2	204.7	0.19
30918.8	650.6	0.14	30270.9	208.4	0.16
30961.9	693.7	0.13	30275.5	213	0.16
30969.5	701.3	0.29	30281	218.5	0.17
30981.1	712.9	0.27	30283.7	221.2	0.16
30991.6	723.4	0.23	30287.4	224.9	0.17
30995.5	727.3	0.13	30292.9	230.4	0.14
31006	737.8	0.11	30294.7	232.2	0.13
31065.7	797.5	0.14	30299.3	236.8	0.07
31069.6	801.4	0.35	30304.84	242.34	0.61
31076.4	808.2	0.14	30335.2	272.7	0.06
31090.9	822.7	0.15	30354.5	292	0.06
31151.9	883.7	0.17	30367.4	304.9	0.15
31166.5	898.3	0.37	30370.2	307.7	0.19
31170.3	902.1	0.3	30372.9	310.4	0.16
31172.3	904.1	0.29	30378.5	316	0.22
31176.1	907.9	0.29	30385	322.5	0.45
31181	912.8	0.24	30394.2	331.7	0.17
31183.9	915.7	0.17	30397.1	334.6	0.08
31186.8	918.6	0.23	30415.4	352.9	0.08
31189.8	921.6	0.14	30446	383.5	0.08
31197.5	929.3	0.13	30453.4	390.9	0.13

Continued on next page

E (cm^{-1})	**E* (cm^{-1})**	**I**	**E (cm^{-1})**	**E* (cm^{-1})**	**I**
31216	947.8	0.1	30455.3	392.8	0.13
31224.8	956.6	0.1	30459.9	397.4	0.12
31248.2	980	0.17	30461.8	399.3	0.18
31251.2	983	0.13	30465.5	403	0.15
31259	990.8	0.35	30468.3	405.8	0.11
31271.7	1003.5	0.1	30862.3	799.8	0.07
31291.2	1023	0.15	30567.9	505.4	0.06
31295.2	1027	0.15	30576.3	513.8	0.05
31300.1	1031.9	0.25	30619.4	556.9	0.17
31341.3	1073.1	0.24	30658.8	596.3	0.08
31346.2	1078	0.13	30692.7	630.2	0.08
31355	1086.8	0.13	30763.5	701	0.09
31374.7	1106.5	0.13	30775.8	713.3	0.1
31380.6	1112.4	0.13	30785.3	722.8	0.12
			30819.5	757	0.12
			30827.1	764.6	0.13
			30830.9	768.4	0.15
			30837.5	775	0.1
			30860.4	797.9	0.09
			30873.7	811.2	0.08
			30887	824.5	0.14
			30890.9	828.4	0.12
			30895.6	833.1	0.1
			30909	846.5	0.1

*relative to 0-0 transition

Table 5.3: Calculated harmonic frequencies of 1,8-naphthalic anhydride and 1,8-naphthalimide in $2^1A_1(\pi\pi^*)$ state. Frequencies have been scaled with a factor of 0.960

	1,8-naphthalic anhydride		**1,8-naphthalimide**	
symm.	**label**	**freq., cm^{-1}**	**label**	**freq.,cm^{-1}**
a_1	1	3140	1	3476
	2	3114	2	3138
	3	3098	3	3111
	4	1773	4	3096
	5	1609	5	1707
	6	1480	6	1608
	7	1446	7	1479
	8	1384	8	1457
	9	1382	9	1384
	10	1310	10	1380
	11	1168	11	1347
	12	1110	12	1186
	13	1059	13	1141
	14	926	14	1061
	15	788	15	933
	16	638	16	788
	17	558	17	669
	18	434	18	560
	19	421	19	445
	20	346	20	421
			21	341
a_2	1	946	1	946
	2	835	2	837
	3	743	3	751
	4	693	4	699
	5	507	5	513
	6	343	6	353
	7	201	7	208
	8	66	8	78
b_1	1	947	1	948
	2	878	2	877
	3	761	3	767
	4	693	4	720
	5	674	5	694
	6	471	6	659
	7	427	7	470
	8	195	8	430
	9	143	9	198
	10	132	10	151
			11	132

Continued on next page

symm.	**label**	**freq., cm^{-1}**	**label**	**freq.,cm^{-1}**
b_2	1	3139	1	3137
	2	3113	2	3110
	3	3096	3	3093
	4	1724	4	1698
	5	1552	5	1553
	6	1451	6	1440
	7	1405	7	1404
	8	1390	8	1392
	9	1226	9	1356
	10	1159	10	1228
	11	1139	11	1184
	12	1057	12	1130
	13	1002	13	1112
	14	980	14	1050
	15	784	15	992
	16	655	16	757
	17	509	17	642
	18	384	18	506
	19	273	19	374
			20	272